MULTIPLE JETS FROM THE HIGH-MASS (PROTO)STELLAR CLUSTER AFGL 5142

Qizhou Zhang,[1] Todd R. Hunter,[1] H. Beuther,[2] T. K. Sridharan,[1]
S.-Y. Liu,[3] Y.-N. Su,[3] H.-R. Chen,[4] and Y. Chen[1]

ABSTRACT

We present studies of the massive protocluster AFGL 5142 in the $J = 2-1$ transition of the CO isotopologues, SO, CH$_3$OH, and CH$_3$CN lines, as well as in the continuum at 225 GHz and 8.4 GHz. The 225 GHz continuum emission reveals at least five dust continuum peaks. The strongest peaks, MM-1 and MM-2, are associated with hot cores with temperatures of 90 ± 20 and 250 ± 40 K, respectively. With similar core mass, the higher temperature and CH$_3$CN abundance in the MM-2 core suggest that it might be at a more evolved stage than the MM-1 core. A total of 22 lines from nine molecules are detected. The line strength varies remarkably in the region. Strong SO emission is found both in molecular outflows and cloud cores. CH$_3$OH emission, on the contrary, is much weaker in molecular outflows, and is detected toward hot cores MM-1 and MM-2, but is absent in the less massive and perhaps less evolved cores MM-3, MM-4, and MM-5. The CO and SO emission reveals at least three molecular outflows originating from the center of the dust core. The outflows are well collimated, with terminal velocities up to 50 km s^{-1} from the cloud velocity. Since jetlike outflows and disk-mediated accretion process are physically connected, the well-collimated outflows indicate that even in this cluster environment, accretion is responsible for the formation of individual stars in the cluster.

Subject headings: H ii regions — ISM: clouds — ISM: individual (AFGL 5142) — ISM: kinematics and dynamics — masers — stars: formation

1. INTRODUCTION

AFGL 5142 is a high-mass star-forming region at a distance of 1.8 kpc (Snell et al. 1988). There are two centers of high-mass star formation in this region: IRAS 05274+3345 exhibits bright near-infrared emission (Hunter et al. 1995) with a far-infrared luminosity of $3 \times 10^3 L_\odot$, but has little dense molecular gas associated with it (Estalella et al. 1993). About 30″ to the east of IRAS 05274+3345 lies a faint centimeter continuum source of about 1 mJy at 3.6 cm that is referred as IRAS 05274+3345 East (Torrelles et al. 1992). If the continuum emission arises from an optically thin, homogeneous H ii region, the flux density is equivalent to that of a zero-age main-sequence (ZAMS) star of spectral type B2 or earlier (Hunter et al. 1995; Torrelles et al. 1992). The source is also associated with emission from dust, dense molecular gas in NH$_3$, CS, HCN, HCO$^+$, CH$_3$OH, and CH$_3$CN (Estalella et al. 1993; Hunter et al. 1995, 1999; Cesaroni et al. 1999; Slysh et al. 1997; Pestalozzi et al. 2005), and H$_2$O, OH, and Class II CH$_3$OH masers (Hunter et al. 1995, 1999; Goddi & Moscadelli 2006); Slysh et al. 1997; Pestalozzi et al. 2005). High-resolution images reveal a cluster of H$_2$O masers distributed in an area of 5″. At a resolution of 3″, a 3 mm continuum core is found with its peak coincident with the centimeter continuum source (Hunter et al. 1999). All the information indicates that IRAS 05274+3345 is a more evolved region, while the active star formation occurs in the dense core 30″ to the east.

Hunter et al. (1995) reported two outflows in the CO 2–1 line: an extended remnant flow in the southeast-northwest orientation, possibly driven by the brightest near-infrared source near IRAS 05274+3345, and a compact active outflow in the north-south orientation originating from the centimeter/dust continuum emission of IRAS 05274+3345 East. This north-south outflow component is also seen in the CO 3–2 line observed with the Caltech

Submillimeter Observatory (CSO; Hunter et al. 1995). Follow-up studies at high angular resolution from the Owens Valley Radio Observatory (OVRO) revealed a well-collimated SiO jet and an HCO$^+$ outflow in the north-south orientation (Hunter et al. 1999). In addition, there appears to be a unipolar outflow in the HCO$^+$ emission at a 35° position angle. Both outflows appear to originate from the 3 mm continuum peak, which is unresolved at 3″ resolution. Copious near-infrared H$_2$ emission knots are associated with the outflow lobes (Hunter et al. 1999; Chen et al. 2005). High-resolution NH$_3$ studies with the Very Large Array (VLA) reveal a compact disklike structure of 1.2″ in size with a large line width of 6.4 km s^{-1} and a velocity gradient over a scale of 2000 AU (Zhang et al. 2002). This NH$_3$ structure coincides with the peak of the centimeter and millimeter emission and was interpreted as a rotating disk surrounding a massive star.

However, with a spatial resolution of 3″, the millimeter observations from OVRO may not resolve close binaries in a cluster environment. In order to further investigate the outflow and the structure and kinematics in the core, we observed the IRAS 05274+3345 East region with the Submillimeter Array (SMA) in CO and its isotopologues, dense gas tracers, and 1.3 mm continuum emission at a resolution of about 1″. In addition, we also obtained the 3.6 cm continuum image from the VLA. The continuum images at 1.3 mm and 3.6 cm indeed reveal multiple emission peaks. The CO and SO emission reveals at least three molecular outflows. In § 2, we present the observational setup. In § 3, we describe the main results revealed in the study. In § 4, we discuss the findings in the context of cluster formation. We conclude in § 5 with the main findings of the investigation.

2. OBSERVATIONS AND DATA REDUCTION

2.1. *SMA*

Observations of AFGL 5142 were carried out with the Submillimeter Array[5] (Ho et al. 2004) on 2004 January 11 with six

[1] Harvard-Smithsonian Center for Astrophysics, Cambridge, MA.
[2] Max Planck Institute for Astronomy, Heidelberg, Germany.
[3] Academia Sinica Institute of Astronomy and Astrophysics, Taipei, Taiwan.
[4] Institute of Astronomy and Department of Physics, National Tsing Hua University, Hsinchu, Taiwan.
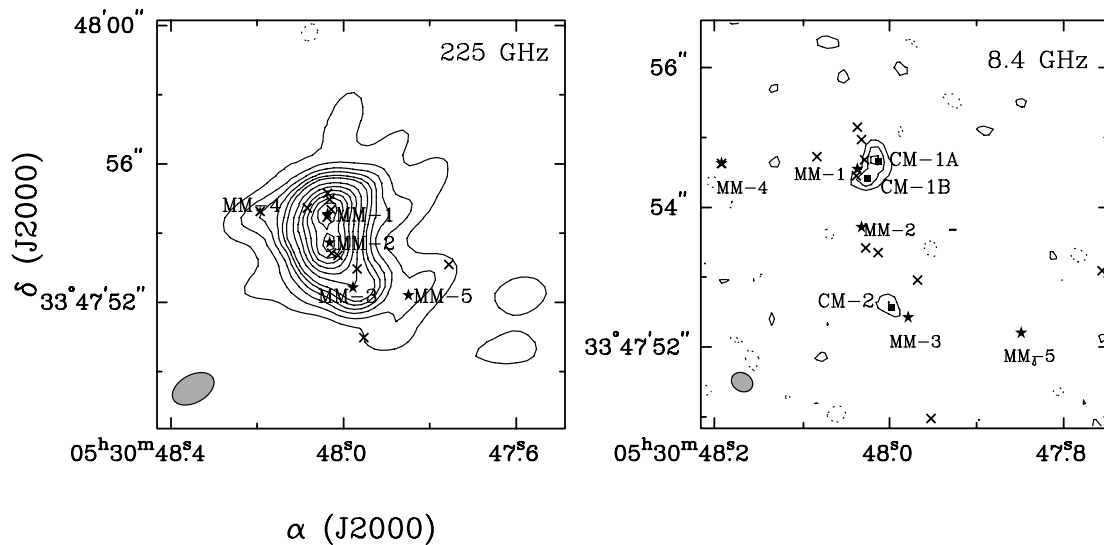
Fig. 1.—Continuum emission toward AFGL 5142 at 225 GHz (1.3 mm) and 8.4 GHz (3.6 cm). The 1.3 mm continuum peaks (MM-1, MM-2, MM-3, MM-4, and MM-5) are marked by stars in both panels. The 3.6 cm continuum peaks (CM-1A, CM-1B, and CM-2) are marked by filled squares in the right panel. The H_2O maser positions from Hunter et al. (1999) are marked by crosses. The contour levels are in steps of 12 mJy beam^{-1} for the 225 GHz image and 0.2 mJy beam^{-1} for the 8.4 GHz image. The size of the synthesized beam is shown at the bottom left corner of each panel.

antennas in the compact configuration and on 2004 February 17 with eight antennas in the extended configuration. The projected baselines of the two array configurations range from 15 to 210 m (11−160 kλ). The double sideband receivers cover 2 GHz bandwidth at intermediate frequencies of 4−6 GHz. The receivers were tuned to the local oscillator (LO) frequency of 225 GHz to capture ^{13}CO 2−1, $C^{18}O$ 2−1, and CH_3CN 12−11 in the lower sideband and ^{12}CO 2−1 in the upper sideband. The digital correlator was configured to provide a uniform channel spacing of 0.8125 MHz ($\sim$1 km s^{-1}) across the entire band. A detailed description of the SMA is given in Ho et al. (2004).

The primary beam of the SMA at this frequency is about 57$''$. The phase center for the observations is α(J2000.0) = 05^{h}30^{m}48.02^s, δ(J2000.0) = 33$°$47$'$54.47$''$. We used quasars 0359+509 and 0555+398 to calibrate time-dependent gains, and we used Jupiter to remove the gain variations across the passband. The flux scale was referenced to the Jovian moon Callisto. The visibility data were calibrated with the IDL superset MIR package[6] developed for the Owens Valley Interferometer. The absolute flux level is accurate to about 15%. After the calibration in MIR, the visibility data were exported to the MIRIAD format for further processing and imaging. The continuum is constructed from the line-free channels in the visibility domain and is further self-calibrated using the clean components of the image as input models. The gain solution from the self-calibration is applied to the spectral line data. The rms in the naturally weighted maps is 4.4 mJy beam^{-1} in the continuum and 90 mJy beam^{-1} per 1.2 km s^{-1} channel in the line data. The synthesized beams of the images vary from 1$''$ to 3$''$ (1700−5100 AU), depending on the weighting of the visibilities in the Fourier transformation. The uncertainty in the absolute position is $\lesssim$0.2$''$, derived from comparing quasar positions from two sidebands.

2.2. VLA

Observations of AFGL 5142 with the Very Large Array[7] were carried out on 2003 June 15 in the A configuration. The corre-

lator was configured in the continuum mode at 3.6 cm with a total bandwidth of 200 MHz. The visibility data were made available to the public through the VLA data archive. The pointing center is the same as that of the SMA. The primary beam of the VLA is about 6$'$ at this frequency. 3C 147 was used as the flux calibrator, and 0443+346 was used as the gain calibrator. The visibility data were calibrated using the AIPS package. The rms in the naturally weighted image is 0.09 mJy beam^{-1}, with a synthesized beam of 0.32$'' \times$ 0.26$''$ (or 510 AU $\times$ 440 AU) at a position angle of 58.6$°$. The uncertainty in the absolute position is better than 0.03$''$, 1/10 of the synthesized beam.

2.3. Supplemental Short-Spacing Information for the ^{12}CO Emission

The shortest projected baseline (11 kλ) in the SMA observations corresponds to a spatial scale of 1.2λ/b, or 20$''$. Here b is the length of the projected baseline. Spatial structures more extended than 20$''$ were not sampled in the SMA observations. This filtering effect can affect the appearance of images of easily excited molecular lines such as CO. To recover the missing short-spacing information in the ^{12}CO 2−1 line, we add the single-dish data obtained from the CSO (Hunter et al. 1995) to the SMA data, following a procedure outlined in Zhang et al. (1995). The CSO spectra have a velocity range from −35 to 30 km s^{-1} and do not cover the entire high-velocity wings detected in the SMA data. However, the highest velocity CO emission appears to be spatially compact; thus, it does not suffer strongly from the missing flux problem.

The combined image of the ^{12}CO 2−1 line, when convolved to the 29$''$ beam of the CSO, recovers about 90% of the flux from the single-dish telescope. The ^{13}CO 2−1 emission from the SMA also appears to miss extended emission around the cloud systemic velocity. For that reason, we avoid interpreting the ^{13}CO image around the cloud systemic velocity.

3. RESULTS

3.1. Continuum Emission

Figure 1 presents the continuum images at 225 GHz (1.3 mm) and 8.4 GHz (3.6 cm) overlaid with the H_2O maser emission

---

[6] Available at http://www.cfa.harvard.edu/~cqi/mircook.html.

[7] The National Radio Astronomy Observatory is operated by Associated Universities, Inc., under cooperative agreement with the National Science Foundation.

TABLE 1
Parameters of Continuum Sources

Name	R.A. (J2000.0)	Decl. (J2000.0)	S_{peak} (mJy beam^{-1})	Mass[a] ($M_\odot$)
CM-1A	05 30 48.014	33 47 54.66	0.65	...
CM-1B	05 30 48.025	33 47 54.41	0.64	...
CM-2	05 30 47.999	33 47 52.57	0.35	...
MM-1	05 30 48.037	33 47 54.55	240	3
MM-2	05 30 48.034	33 47 53.72	230	3
MM-3	05 30 47.979	33 47 52.42	84	2
MM-4	05 30 48.193	33 47 54.62	35	0.9
MM-5	05 30 47.849	33 47 52.20	27	0.8

Notes.—There appears to be an offset of 0.2″ between the 225 GHz data and the 8.4 GHz and NH$_3$ data from the VLA. This offset is within the calibration error in the 225 GHz data set. Minor millimeter peaks of less than 6 σ are not reported here. Units of right ascension are hours, minutes, and seconds, and units of declination are degrees, arcminutes, and arcseconds.

[a] We assume a dust temperature of 45 K for MM-1 and MM-2, based on the estimate in Hunter et al. (1999), and 20 K for MM-3, MM-4, and MM-5, based on the NH$_3$ observations (Zhang et al. 2002).

from Hunter et al. (1999). The VLA image reveals three continuum peaks. The two peaks CM-1A and CM-1B in the north are separated by 0.2″. They have a peak intensity of 0.65 and 0.64 mJy beam^{-1}, respectively, detected well above the 1 σ rms of 0.09 mJy beam^{-1}. These two peaks were not resolved in previous observations with the VLA. The integrated flux of the two sources is 1.4 mJy, consistent with observations at lower resolution (Hunter et al. 1999). There appears to be an additional centimeter continuum source 2″ to the south of CM-1A and CM-1B. This source, labeled as CM-2, has a flux intensity of 0.35 mJy beam^{-1}. CM-2 was not reported in the previous observations, possibly due to confusion from the extended emission.

At a resolution of 1.3″ × 0.8″, the 225 GHz continuum image reveals two dominant peaks separated by about 1″. The northern peak, MM-1, coincides with two 8.4 GHz continuum peaks, CM-1A and CM-1B. The southern peak, MM-2, does not have any counterpart at 8.4 GHz at a 1 σ sensitivity of 0.09 mJy beam^{-1}.

In addition to MM-1 and MM-2, there exist other millimeter continuum peaks. The extension toward the southwest from MM-2, labeled as MM-3, is close to the centimeter emission feature CM-2. The H$_2$O maser feature 3″ to the east of MM-1 coincides with a dust peak that we label as MM-4. Furthermore, a dust emission peak lies about 2″ west of MM-3. We refer to this peak as MM-5. The values of the flux density per beam at the continuum peaks are listed in Table 1. The expected contribution from the ionized gas at millimeter and submillimeter wavelengths is $\lesssim$1 mJy (Hunter et al. 1999). Thus, dust emission dominates the 1.3 mm continuum flux of all the sources, and it likely does so to wavelengths as long as ~3 mm. Because of a lack of high-resolution images at more than one wavelength, the emissivity index of the dust emission at each peak cannot be evaluated. Instead, we convolve the continuum map at 225 GHz to the same synthesized beam as the 88 GHz map in Hunter et al. (1999) to estimate an average emissivity index for the region. We obtain a peak flux density of 0.62 Jy at 225 GHz. Comparing with the flux density of 0.038 Jy measured in the same beam at 88 GHz, we derived an index of $\alpha = 3$, or an emissivity index of $\beta = 1$. This value of β is smaller than the typical value of 2 for the interstellar dust, but it is consistent with the value in a similar object, IRAS 20126+4104 (Cesaroni et al. 1999). Using the Hildebrand dust opacity law (Hildebrand 1983), we find a dust opacity per unit dust mass of κ_0(225 GHz) = 1.8 cm^{-2} g^{-1}. For a dust temperature of 45 K, based on the estimate in Hunter et al. (1999) and an integrated flux of 1.5 Jy, we obtain a total mass of

50 $M_\odot$ in the region. We note that this mass is smaller than the value of 145 $M_\odot$ derived from the 3 mm flux in Hunter et al. (1999). The difference is attributed mostly to the dust opacity: Hunter et al. (1999) adopted an opacity of 0.5 cm^{-2} g^{-1} at 230 GHz, which is about 30% of the opacity used in this paper, and hence their calculations resulted in a higher mass estimate. With the Hildebrand dust opacity, the circumstellar mass within one synthesized beam (~1800 AU) estimated from the 225 GHz peak flux is 3 $M_\odot$ for both MM-1 and MM-2. The kinetic temperature toward MM-3, MM-4, and MM-5 is about 20 K on the basis of the NH$_3$ studies (Zhang et al. 2002). At that temperature, we derive a mass of 2 $M_\odot$ for MM-3, 0.9 $M_\odot$ for MM-4, and 0.7 $M_\odot$ for MM-5, respectively.

As shown in Figure 1, MM-1 appears to coincide with CM-1A and CM-1B, and MM-3 appears to coincide with CM-2. The maximum offset among the centimeter and millimeter counterparts is <0.2″, which is within the uncertainty in the astrometry of the SMA image. Therefore, the spatial displacement between the millimeter and centimeter peaks may not be physical. The centimeter emission likely arises either from the H II region due to ionization of massive stars or from the ionized wind emission in outflows. In general, the thermal free-free emission from the H II region tends to have a negative spectral index α (defined as $F_\nu \propto \nu^\alpha$) of about -0.1 in the optically thin limit. On the other hand, the emission from the ionized wind tends to have a positive spectral index of about 0.6 (Anglada et al. 1998). Without images of similar resolution at other centimeter wavelengths, we cannot access the physical nature of the emission. If the emission arises from the optically thin and homogeneous ionized gas in the H II region, the flux density from the three centimeter peaks corresponds to ZAMS stars of spectral type B3–B2. However, as discussed in § 4.1, the 3.6 cm emission is probably due to ionized wind emission from outflows.

3.2. Line Emission

3.2.1. Line Spectroscopy

Figure 2 shows the SMA spectra in the lower sideband and the upper sideband toward the positions of MM-1, MM-2, MM-3, and the redshifted peak of outflow A (marked with a triangle in Fig. 3). The data are cleaned by subtracting the continuum emission constructed from the line-free channels in the visibility domain and are then imaged with robust weighting, resulting in a synthesized beam of 1.3″ × 0.8″ at a position angle of $-60°$. Thus, the spectra taken from the three dust continuum peaks are spatially resolved from each other. In order to increase the signal-to-noise ratio (S/N), the spectrum toward outflow A is made with natural weighting and a spatial tapering of 3″, resulting in a resolution of 4.3″ × 3.6″ at a position angle of $-80°$.

Similarly to other massive star-forming regions (Beuther et al. 2004a, 2004b), multiple molecular lines are detected in the AFGL 5142 region. We detect 22 spectral lines/components from the ^{12}CO, ^{13}CO, C^{18}O, CH$_3$CN, CH$_3$OH, SO, HNCO, OCS, and H$_2^{13}$CO molecules (see Table 2). The energy levels of the lines range from 17 K for CO to 579 K for CH$_3$OH, with critical densities from 10^2 cm^{-3} to 10^7 cm^{-3}. These lines sample a wide range of physical and chemical conditions in the region. The peak in the ^{12}CO 2–1 line appears to be weaker than that of the ^{13}CO line. This is likely due to high optical depths near the cloud local standard of rest (LSR) velocity and to extended emission missed by the interferometer.

As shown in Figure 2, the strength of the molecular lines varies significantly in this region. ^{12}CO and SO are the only molecular lines detected toward all four positions. MM-1 and MM-2 appear to emit in nearly all the molecular lines identified in the region, including the hot-core molecules CH$_3$CN and CH$_3$OH. MM-3, a
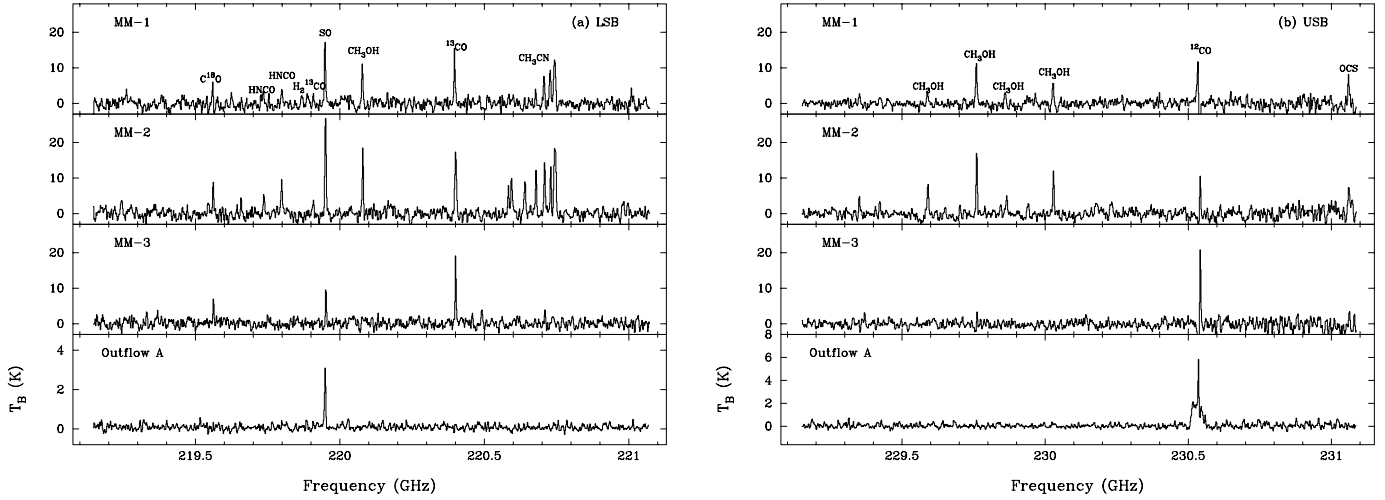
Fig. 2.—Line spectra toward MM-1, MM-2, MM-3, and the redshifted peak in outflow A (the filled triangle in the top right panel of Fig. 3) for the lower sideband (LSB) and the upper sideband (USB). The spectra for the millimeter continuum sources are from images with a resolution of $1.3'' \times 0.8''$ (the conversion factor from Jy beam^{-1} to kelvins is then 17 K Jy^{-1}). The spectrum for the outflow position is made with natural weighting and tapering of visibilities, resulting in an angular resolution of $4.0'' \times 3.3''$ (the conversion factor from Jy beam^{-1} to kelvins is then 1.9 K Jy^{-1}).

faint millimeter source with a mass similar to that of MM-1 and MM-2, is not detected in any of these hot-core molecules. This suggests that the MM-3 core has a lower gas temperature than the MM-2 and MM-1 cores. The presence of SO toward the outflow indicates that the SO abundance is enhanced greatly in the outflow as compared to the core. Table 2 lists the fluxes and line widths of the molecular lines detected toward MM-1 and MM-2.

3.2.2. Line Emission from the Cores

Figure 3 shows the images of the velocity-integrated flux from ^{13}CO $J = 2-1$, $C^{18}O$ $J = 2-1$, SO 6_5-5_4, CH$_3$OH $8_{-1,8}-7_{0,7}$ E

at 229.759 GHz, OCS $J = 19-18$, and HNCO $10_{0,10}-9_{0,9}$ at 219.798 GHz. Emission from all the molecules presented here is seen toward the cores surrounding MM-1 and MM-2. The ^{13}CO emission around the cloud velocity appears to be extended and likely suffers from a missing large-scale component. Thus, we do not discuss the emission in detail. The SO emission reveals an extended component corresponding to molecular outflows, and we will interpret these data in § 3.2.3. The emission from OCS and HNCO is associated with the dense cores surrounding MM-1 and MM-2 only and shows the most compact structure. The CH$_3$OH emission likely arises from both dense cores and outflows.

TABLE 2
Lines Detected in the Hot Cores

Frequency (GHz)	Line	E_{upper} (K)	MM-1		MM-2	
			S (K)	FWHM (km s^{-1})	S (K)	FWHM (km s^{-1})
219.560	C^{18}O 2−1	16	9.4	2.9	11.7	4.4
219.733	HNCO 10$_{2,9}$−9$_{2,8}$	230	4.5	...	8.0	4.8
219.737	HNCO 10$_{2,8}$−9$_{2,7}$	230	4.5	...	8.0	4.8
219.798	HNCO 10$_{0,10}$−9$_{0,9}$	59	4.8	5.8	12.4	4.9
219.909	H$_2^{13}$CO 3$_{1,2}$−2$_{1,1}$	23	3.4	3.7	5.4	3.7
219.949	SO 6$_5$−5$_4$	35	20.2	5.6	30.0	5.8
220.079	CH$_3$OH 8$_{0,8}$−7$_{1,6}$	96	14.2	4.9	25.3	3.6
220.399	^{13}CO 2−1	16	24.0	2.2	20.4	5.8
220.584	HNCO 10$_{1,9}$−9$_{1,8}$	59	...	...	11.4	4.9
220.594	CH$_3$CN 12$_6$−11$_6$	326	4.7	4.7	13.1	4.0
220.641	CH$_3$CN 12$_5$−11$_5$	248	4.6	4.7	10.7	4.0
220.679	CH$_3$CN 12$_4$−11$_4$	184	5.4	4.7	16.3	4.0
220.709	CH$_3$CN 12$_3$−11$_3$	134	14.6	4.7	17.2	4.0
220.730	CH$_3$CN 12$_2$−11$_2$	98	10.3	4.7	20.1	4.0
220.743	CH$_3$CN 12$_1$−11$_1$	76	10.0	4.7	22.3	4.0
220.747	CH$_3$CN 12$_0$−11$_0$	69	12.3	4.7	24.1	4.0
229.589	CH$_3$OH 15$_{4,11}$−16$_{3,13}$ E	374	4.2	5.3	10.0	6.0
229.759	CH$_3$OH 8$_{-1,8}$−7$_{0,7}$ E	89	12.3	6.3	22.7	4.4
229.864	CH$_3$OH 19$_{5,15}$−20$_{4,16}$ $A+$	579	3.4	...	6.0	6.0
230.027	CH$_3$OH 3$_{-2,2}$−4$_{-1,4}$ E	39	6.0	5.8	15.8	4.0
230.538	^{12}CO 2−1[a]	17	40.0	8.6	40.0	8.6
231.061	OCS 19−18	111	7.2	5.8	7.3	7.5

Note.—We listed lines detected above the 5 σ level.
[a] The CO 2−1 spectrum is self-absorbed. The Gaussian fitting is uncertain.
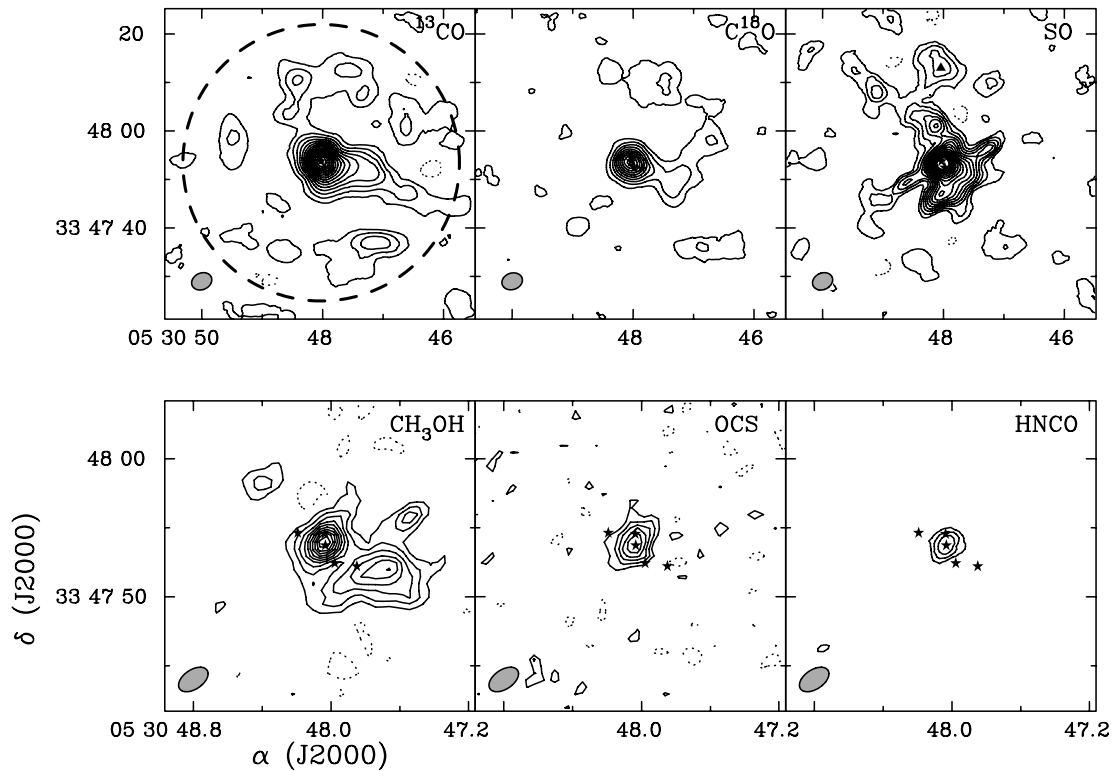
FIG. 3.—Images of the velocity-integrated flux of $^{13}CO\ J = 2-1$, $C^{18}O\ J = 2-1$, SO 6_5-5_4, $CH_3OH\ 8_{-1,8}-7_{0,7}\ E$, OCS $J = 19-18$, and HNCO $10_{0,10}-9_{0,9}$ for AFGL 5142. The range of the integration covers the entire velocity of the line. The stars mark the positions of the millimeter continuum peaks MM-1, MM-2, MM-3, MM-4, and MM-5. The triangle in the SO panel marks the position of the spectrum from outflow A that is shown in Fig. 2. The contour levels are in steps of 3 Jy km s^{-1} beam^{-1}, starting from 3 Jy km s^{-1} beam^{-1}, for the $^{13}CO\ J = 2-1$ line; in steps of 2 Jy km s^{-1} beam^{-1}, starting from 2 Jy km s^{-1} beam^{-1}, for the SO 6_5-5_4 and $C^{18}O\ J = 2-1$ lines; and in steps of 1 Jy km s^{-1} beam^{-1}, starting from 1 Jy km s^{-1} beam^{-1}, for the $CH_3OH\ 8_{-1,8}-7_{0,7}\ E$, OCS $J = 19-18$, and HNCO $10_{0,10}-9_{0,9}$ lines. The size of the primary beam (57$''$) is marked by the dashed circle in the top left panel. The size of the synthesized beam is shown by the shaded ellipse at the bottom left corner of each panel.

The $CH_3CN\ J = 12-11$ line also displays compact emission similar to that of OCS and HNCO. Figure 4 presents the integrated CH_3CN emission and the spectra toward MM-1 and MM-2. At a resolution of $1.3'' \times 0.8''$, the two millimeter continuum sources are resolved from each other in the CH_3CN emission. As shown in the CH_3CN spectra, the emission from MM-2 is much stronger than that from MM-1, thus dominating the integrated flux in Figure 4. The hyperfine transitions of the $K = 0-6$ com-

ponents of CH_3CN with energy levels from 69 to 326 K are detected. The emission from the higher K components of CH_3CN toward MM-1 is much weaker than that toward MM-2. This indicates that MM-1 has a lower temperature than MM-2. Despite the difference in statistical weights by a factor of 2, the $K = 2$ and 3 components from both sources have similar brightness temperatures, indicating a moderate optical depth in the lines. Assuming LTE, we fit the CH_3CN line profiles using a radiative transfer
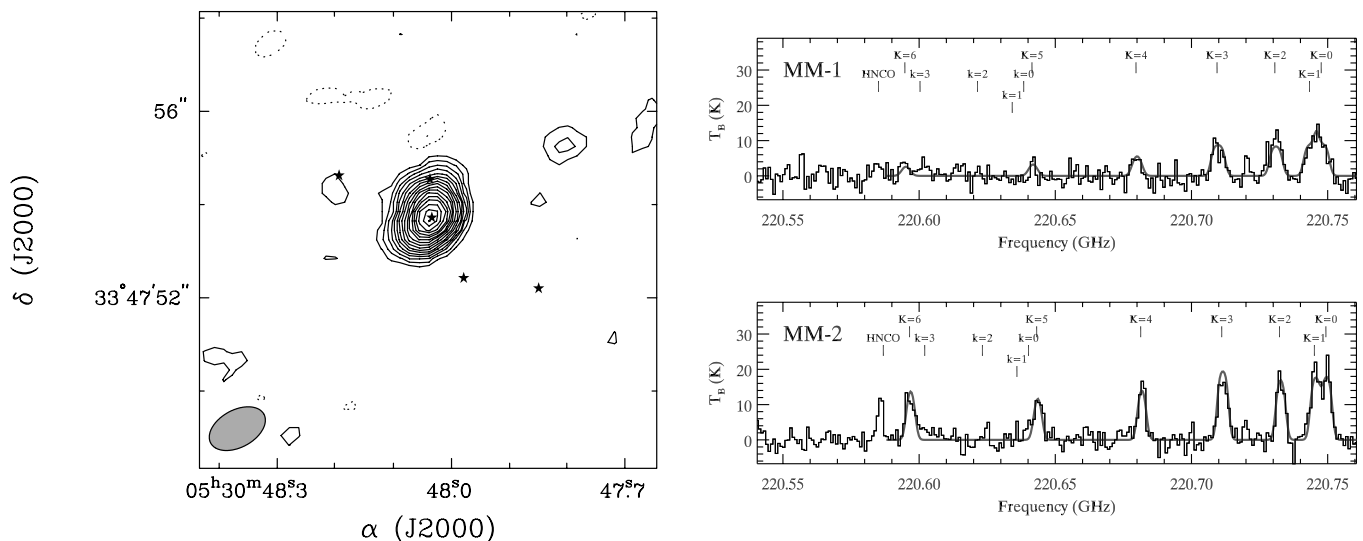

FIG. 4.—Left: Integrated emission of the $CH_3CN\ J = 12-11$ line. The contour levels are in steps of 2 Jy km s^{-1} beam^{-1}. The stars mark the positions of the millimeter continuum peaks MM-1, MM-2, MM-3, MM-4, and MM-5. The size of the synthesized beam is shown by the shaded ellipse at the bottom left corner. Right: Observed (thin black lines) and model (thick gray lines) spectra toward the positions of MM-1 and MM-2.
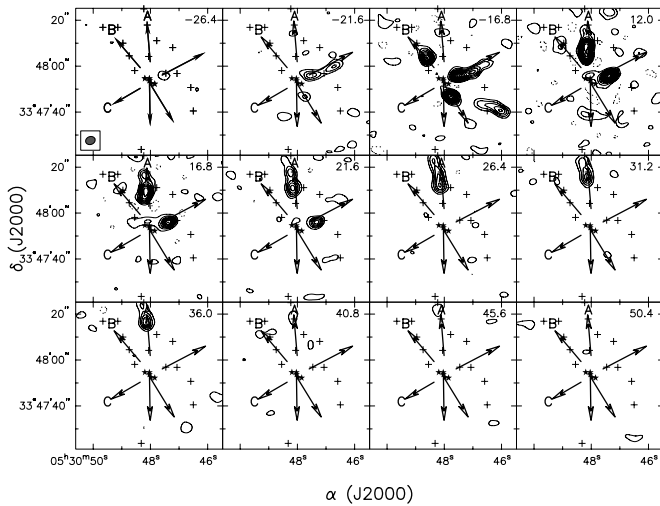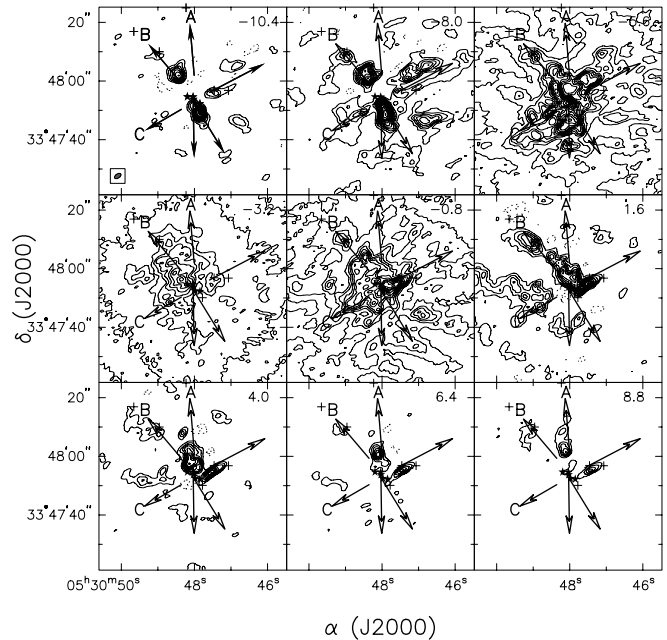
Fig. 5a

Fig. 5b

Fig. 5.— Emission toward AFGL 5142 in the ^{12}CO 2−1 line. The stars mark the positions of the millimeter continuum peaks MM-1, MM-2, MM-3, MM-4, and MM-5. The plus signs denote the near-infrared H$_2$ emission knots (Hunter et al. 1999). Arrows mark the three molecular outflows A, B, and C. The corresponding velocity range of the ^{12}CO emission is labeled at the top right corner of each panel. The size of the synthesized beam is shown by the shaded ellipse at the bottom left corner of the first panel. (a) High-velocity ^{12}CO 2−1 emission from the SMA data alone. The contour levels are in steps of 0.3 mJy beam^{-1}. (b) Low-velocity ^{12}CO 2−1 emission from combined SMA and CSO data. The contour levels are in steps of 0.6 mJy beam^{-1}.

model in a uniform, isothermal spherical core (Chen et al. 2006). The emergent spectrum depends on the gas temperature, density, central velocity, line width, and the size of the emitting region. By varying these parameters, we obtain the best fit by minimizing the χ^2 between the observed and model spectra. This approach takes into account the optical depth effect, thus producing a better fit to the line profiles of all the K components than that obtained using the energy diagram, which assumes optically thin emission (e.g., Zhang et al. 1998). Figure 4 shows the CH$_3$CN $J =$ 12−11 lines reproduced from the model: the match between the observed and model spectra is reasonable. The fitting yields $V_{\rm LSR} = -1 \pm 0.2$ km s^{-1}, FWHM = 4.7 ± 0.5 km s^{-1}, $T_K =$ 90 ± 20 K, $n_{\rm CH_3CN} = 1.3 \pm 0.7$ cm^{-3}, and the core radius $R = 440 \pm 80$ AU for MM-1 and $V_{\rm LSR} = -3.4 \pm 0.1$ km s^{-1}, FWHM = 4.0 ± 0.2 km s^{-1}, $T_K = 250 \pm 40$ K, $n_{\rm CH_3CN} = 6 \pm 4$ cm^{-3}, and $R = 380 \pm 80$ AU for MM-2. The central velocity of the CH$_3$CN cores toward MM-1 and MM-2 differs by 2.4 km s^{-1}. This difference, also seen in the SO and CH$_3$OH emission, confirms that both dust continuum sources contribute to the observed CH$_3$CN emission.

The temperature and density derived from CH$_3$CN reveal that the physical conditions in the MM-1 and MM-2 cores are different. MM-2 has a much higher temperature and column density than MM-1. As shown in Table 2 and Figures 2 and 4, the higher K components of the CH$_3$CN line toward MM-1 are weaker than those toward MM-2. In addition, emission from higher energy levels of CH$_3$OH and HNCO are much weaker or are not detected toward MM-1. These measurements are consistent with a lower temperature and a lower CH$_3$CN density toward MM-1. From the dust emission, MM-1 and MM-2 have a similar peak flux. At the assumed dust temperature of 45 K, the mass in both cores (3 $M_\odot$) yields a mean H$_2$ density of 1.5×10^8 cm^{-3} averaged over the volume of the synthesized beam (1800 AU). Thus, the fractional abundance of CH$_3$CN relative to H$_2$ is 1×10^{-8} and 4×10^{-8} toward MM-1 and MM-2, respectively. Both values are 2 orders

of magnitude higher than the abundance in dark clouds (Herbst & Leung 1990), similar to that in the hot core (Wilner et al. 1994). The abundance in the MM-2 core is higher than in the MM-1 core. On the basis of the fitting of the CH$_3$CN spectra, MM-2 has a gas temperature 2.5 times that in the MM-1 core. If the gas and dust reach an equilibrium temperature, the mass and hence the average H$_2$ density in MM-2 should be smaller than that in MM-1. This would result in an even higher CH$_3$CN abundance toward MM-2. The higher CH$_3$CN abundance in MM-2 is likely the result of higher temperature in the MM-2 core, which enhances the production of CH$_3$CN.

In addition to CH$_3$CN, emissions from SO, OCS, HNCO, and CO isotopologues are also detected toward MM-1 and MM-2. The central velocity of the emission from these molecular lines is centered around −1 and −3.4 km s^{-1} for MM-1 and MM-2, respectively, similar to that in the CH$_3$CN emission. As shown in § 3.2.3, the SO and CH$_3$OH emission can arise from outflows. The agreement of the line velocity indicates that the SO and CH$_3$OH emission toward MM-1 and MM-2 arise from the dense cores.

Unlike MM-1 and MM-2, far fewer molecular lines are detected toward MM-3. In particular, CH$_3$CN, CH$_3$OH, OCS, and HNCO are all absent (at a 1 σ sensitivity of 0.09 Jy), despite the presence of faint 8.4 GHz emission. The absence of these lines also indicates that MM-3 is at a lower temperature than that of the MM-1 and MM-2 cores.

3.2.3. Molecular Outflows

Figure 5 presents the channel maps of the ^{12}CO 2−1 line. Since the single-dish CO 2−1 data from the CSO do not cover the high-velocity wing emission, the combined SMA and CSO data have a limited velocity coverage from −35 to 30 km s^{-1}. The CO emission at $\Delta V > 15$ km s^{-1} is compact and therefore subject to little missing flux. Thus, we show in Figure 5a the high-velocity emission obtained from the SMA alone, whereas Figure 5b presents
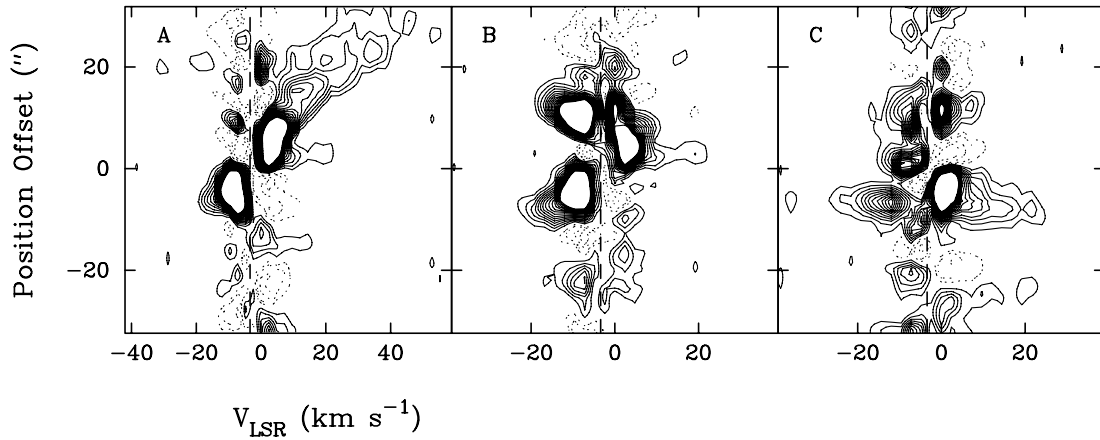
Fig. 6.—Position-velocity diagram of the ^{12}CO 2–1 emission. The CO data are from the SMA alone. The cuts are along the axes of outflows A, B, and C, with position offset at MM-2. The contour levels are in steps of 0.4 Jy beam^{-1}. The vertical dashed lines mark the cloud systemic velocity of -3.9 km s^{-1}.

the low-velocity CO emission from the combined SMA and CSO data. From the CO emission, one can immediately identify an outflow in the north-south direction. The CO 2–1 emission from the CSO (Hunter et al. 1995) peaks at -3.9 km s^{-1}. At the redshifted velocities of 10–48 km s^{-1}, there exists high-velocity gas to the north of the millimeter continuum peaks at a position angle of $5°$. The well-collimated CO emission is detected at up to 50 km s^{-1} from the cloud systematic velocity and extends for up to $30''$ from the millimeter continuum sources. The velocity of the redshifted CO emission increases with the distance from the millimeter continuum sources. The redshifted lobe appears to be clumpy. The peak of the CO clumps is not aligned along the outflow axis and spans an angle of $\sim 5°$ with respect to the dust continuum peaks (see channels from 12 to 45 km s^{-1} in Fig. 5a). The blueshifted side of the outflow extends about $5''$ to the south from the millimeter continuum peaks, with the CO emission detected at up to -13 km s^{-1}. This outflow, referred as outflow A, coincides spatially with the high-velocity SiO outflow reported in Hunter et al. (1999).

Additional high-velocity CO emission suggests the presence of other outflows. At the blueshifted velocities of -14 to -26 km s^{-1}, the CO emission at a position angle of $35°$ identifies outflow B. The lobe to the southwest of the millimeter continuum sources is mainly blueshifted, with CO emission detected up to -22 km s^{-1} from the cloud velocity. The lobe to the northeast exhibits both blue- and redshifted emission from -18 to 15 km s^{-1}. Weak CO emission is detected about $30''$ southwest of the millimeter continuum peaks. The possible third outflow, outflow C, originates from the millimeter core at a position angle of $-60°$. The lobe to the northwest of the millimeter continuum peaks has a bifurcated structure at -8 km s^{-1}, extending $20''$ to the northwest. Higher velocity emission of ± 25 km s^{-1} is seen toward one side of the shell. The lobe to the southeast has a lower velocity, with a jetlike feature seen in the -8 km s^{-1} channel.

Furthermore, there appear to be additional high-velocity features that may arise from other outflows. For example, the CO emission around $[-15'', -15'']$ from MM-2 seen at velocity channels of -16.8 and -10.4 km s^{-1} does not align with any of the three outflows identified and may trace a fourth outflow in the region.

Figure 6 presents the position-velocity plots of the three outflows identified above. To show the full velocity extent of the outflows, we use the image from the SMA data only. The negative contours (Fig. 6, dotted lines) near the cloud velocity arise from the effect of the missing short-spacing flux. Figure 6 reveals that the maximum velocity in outflow A increases with distance from

the driving source. This "Hubble" law relation has been seen in molecular outflows toward both high- and low-mass stars (Su et al. 2004; Lada & Fich 1996; Gueth & Guilloteau 1999). Outflows B and C show rather complex velocity structures, with both blue- and redshifted high-velocity gas toward the same side of the lobes. This may indicate additional outflows in the region.

Figure 7 shows the channel maps of the SO 6_5–5_4 transition. SO is present in dark clouds (Swade 1989), and its abundance is enhanced in outflows (Bachiller et al. 2001; Viti et al. 2003). The process involves the photoevaporation of sulfur-bearing molecules such as H_2S from dust grains near shocks. The gas-phase H_2S then reacts with OH and O_2 to produce SO and SO_2. Strong SO emission is detected toward the CO outflows in AFGL 5142, but at velocities much closer to the cloud velocity: the SO emission is detected within a velocity range of -15 to 8 km s^{-1}, while the CO emission is seen between -26 and 50 km s^{-1}. Despite the
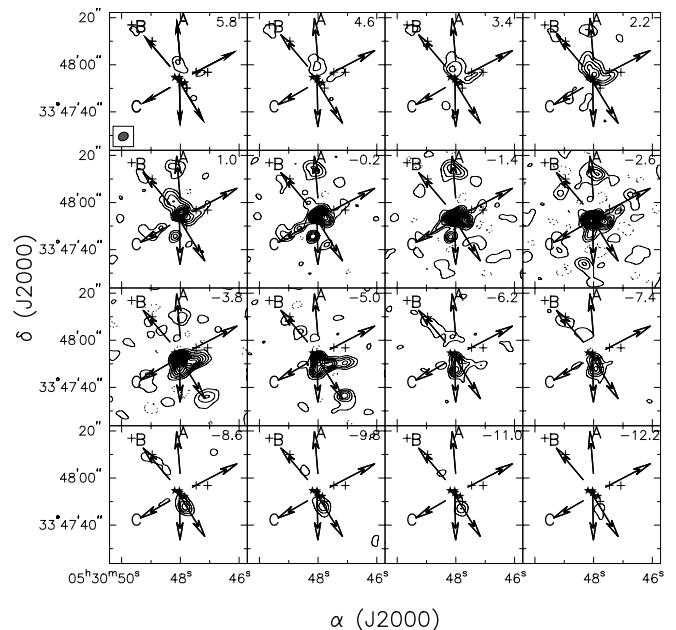

Fig. 7.—Channel maps of the SO 6_5–5_4 line. The contour levels are in steps of 0.4 Jy beam^{-1}. The stars mark the positions of the millimeter continuum peaks MM-1, MM-2, MM-3, MM-4, and MM-5. The plus signs denote the near-infrared H_2 emission knots (Hunter et al. 1999). Arrows mark the three molecular outflows A, B, and C. The size of the synthesized beam is shown by the shaded ellipse at the bottom left corner of the top left panel.

Fig. 8.—Channel maps of the CH$_3$OH $8_{-1,8}$–$7_{0,7}$ E line. The contour levels are in steps of 0.4 Jy beam^{-1}. The stars mark the positions of the millimeter continuum peaks MM-1, MM-2, MM-3, MM-4, and MM-5. The plus signs denote the near-infrared H$_2$ emission knots (Hunter et al. 1999). Arrows mark the three molecular outflows A, B, and C. The size of the synthesized beam is shown by the shaded ellipse at the bottom left corner of the top left panel.
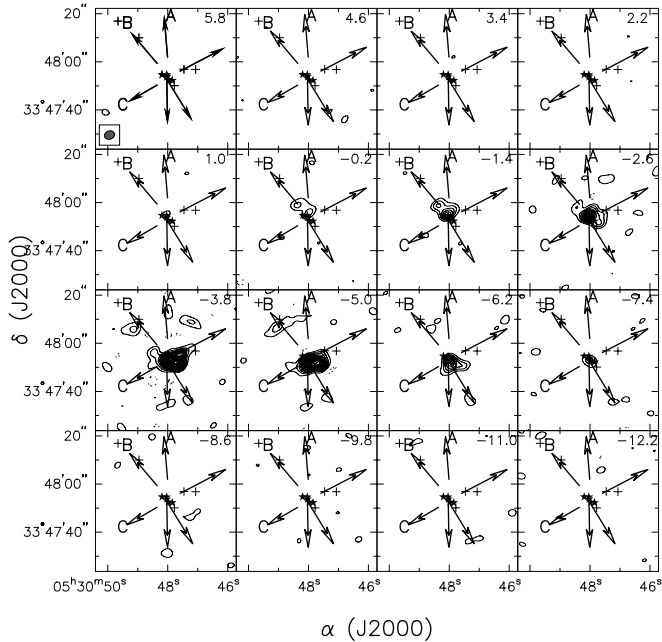
velocity difference from the CO emission, SO emission appears in all three molecular outflows. Outflow A is seen in both the redshifted (-3.8 to 5.8 km s^{-1}) and blueshifted emission (-3.8 to -7.4 km s^{-1}). The spatial extent of the blueshifted and redshifted lobes is similar to that of the CO outflow. Outflow B is clearly seen in SO as well: the redshifted emission in the northeast is detected from -8.6 to 5.8 km s^{-1}, while the blueshifted emission to the southwest is seen from -3.8 to -12.2 km s^{-1}. For outflow C, the SO emission is mostly seen from 2.2 to -8.6 km s^{-1} for the lobe in the southeast and from 5.8 to -2.6 km s^{-1} for the lobe in the northwest.

In addition to SO, the CH$_3$OH emission is detected in the outflows as well. Although CH$_3$OH abundance is low ($<10^{-9}$) in dark clouds, UV radiation from outflow shocks can release CH$_3$OH from dust grains and enhance the CH$_3$OH abundance in molecular outflows (Bachiller et al. 2001; Viti & Williams 1999). Figure 8 presents the channel maps of the CH$_3$OH transition $8_{-1,8}$–$7_{0,7}$ E. The strongest emission is detected along outflow B at velocity channels from -0.2 to -7.4 km s^{-1}. In addition, an extension to the northwest from MM-1, MM-2, and MM-3 appears to be associated with outflow C. In general, the CH$_3$OH emission in the outflow is much weaker than the SO emission and appears at lower velocities than the CO and SO emissions do. Furthermore, the CH$_3$OH emission does not always coincide with the SO emission spatially.

From the CO emission, we estimate the mass and momentum in the outflows. Many studies of molecular outflows assumed optically thin CO emission when estimating outflow parameters. In some cases, an average value of 10 for the ratio of ^{12}CO to ^{13}CO is assumed to correct for the optical depth effect (Choi et al. 1993). However, the opacity is in general a function of velocity. As shown in Su et al. (2004), the CO can be optically thick even in high-velocity wings. The simultaneous observations of ^{12}CO and ^{13}CO with the SMA allow us to investigate the CO optical depth in the outflow. Although ^{13}CO suffers from missing flux

TABLE 3
Outflow Parameters

Outflow	P.A. (deg)	V_{max}[a] (km s^{-1})	T_{dyn}[b] (10^4 yr)	Mass ($M_\odot$)	Momentum ($M_\odot$ km s^{-1})	Energy (10^{45} ergs)
A...........	5	50	0.5	2.5	12	1.1
B...........	35	25	1	3.0	20	2.0
C...........	-60	25	1	3.0	20	2.0

Note.—Parameters are not corrected for orientation of the outflow.
[a] Terminal velocity detectable at an rms of 0.09 Jy.
[b] Dynamic timescale computed from l/V_{max}, where l is the length of the outflow and V_{max} is the terminal velocity of the outflow.

near the cloud velocity, the channel images suggest that this effect is negligible for emission with $\Delta V > 4$ km s^{-1}. By examining the emission ratios, we found that the CO optical depth varies from 4 to 15 in the line wings at 5–12 km s^{-1} from the cloud velocity. Making appropriate corrections for the opacity, we find a total mass, momentum, and energy of 5.9 $M_\odot$, 38 $M_\odot$ km s^{-1}, and 3.4×10^{45} ergs, respectively, for the redshifted CO emission from 1.6 to 50 km s^{-1}. Similarly, we integrate the blueshifted CO emission from -8 to -40 km s^{-1} and find a mass, momentum, and energy in the outflow of 5.7 $M_\odot$, 32 $M_\odot$ km s^{-1}, and 2.5×10^{45} ergs, respectively. There are about equal amounts of mass in the three outflows: 2.5, 3, and 3 $M_\odot$ in outflows A, B, and C, respectively. The momenta in the outflows are from 12 to 20 $M_\odot$ km s^{-1}. The dynamic timescales of the outflows, computed from l/V_{max}, are about 10^4 yr. Here l and V_{max} are the maximum length and velocity of the outflow, where the CO emission is detectable at an rms of 0.09 Jy. The outflow parameters for the three outflows are listed in Table 3. Due to the existence of additional high-velocity features, the masses from the three outflows do not add up to the total outflow mass for the entire region.

4. DISCUSSION

4.1. *Nature of the Continuum Sources*

The presence of multiple continuum peaks and a group of H$_2$O masers indicates a deeply embedded cluster in formation. Both MM-1 and MM-2 give rise to CH$_3$CN emission with rotational temperatures of 90 and 250 K, respectively. Although nearby low-mass protostars may excite hot core–type molecular emission (Ceccarelli et al. 2000; Kuan et al. 2004; Chandler et al. 2005), the emission may not be detectable at larger distances. The protostars that produce heating toward MM-1 and MM-2 and the CH$_3$CN emission are likely to be massive. Scoville & Kwan (1976) derived a relation between the dust temperature and the luminosity of the star:

$$T_D = 65 \left(\frac{0.1 \text{ pc}}{r} \right)^{2/(4+\beta)} \left(\frac{L_{star}}{10^5 \, L_\odot} \right)^{1/(1+\beta)} \left(\frac{0.1}{f} \right)^{1/(4+\beta)} \text{ K.}$$

Here β is the power-law index of the dust emissivity at the far-infrared wavelengths, $f = 0.08$ cm^2 g^{-1} is the value of the dust emissivity at 50 μm, and r is the distance from the star. The dust temperature derived from the fitting to the spectral energy distribution (SED) using a graybody assumption gives a dust temperature of 45 K (Hunter et al. 1999). This value corresponds to the average temperature over $>20''$ scales. At scales of $1''$, dust temperatures can probably reach as high as 250 K, the gas temperature derived from the CH$_3$CN emission, if the gas and dust reach thermal equilibrium in the high-density environment. With $T_D = 45$–200 K, $r = 900$ AU as the size of the dust emission,

and $\beta = 1$, we estimate the luminosity of the star to be from 4×10^3 to $7 \times 10^4 \, L_\odot$. Thus, both protostars are likely to be massive, based on their luminosity. MM-2, with a higher temperature and CH_3CN abundance, may be more evolved than the source embedded in the MM-1 core.

The central velocity of the molecular gas in the two hot cores is offset by 2.4 km s^{-1}. If MM-1 and MM-2 are in a binary, the binding mass of the system is 10/ sin $i \, M_\odot$, where i is the inclination angle of the orbit. The mass in both cores adds up to 6 $M_\odot$. If the two protostars are early B types, as suggested by the presence of hot cores, the combined stellar mass can be up to 20 $M_\odot$. Therefore, the total mass in the stars and circumstellar material is large enough to host the binary. If so, the projected separation of the two stars is 1700 AU, with an orbital period of about 10^4 yr.

Dynamical interactions between members in a protobinary system can cause outflow precession. The CO peaks toward the redshifted lobe of outflow A exhibit misalignment along the outflow axis, which is consistent with a precessing jet. Jet precession has been reported in protostellar outflows associated with both low- and high-mass young stars (Zhang et al. 2000; Shepherd et al. 2000). It appears that the precession of $5°$ in outflow A is much smaller than the $20°–45°$ reported in some of the other protostellar systems, such as IRAS 20126+4104 (Shepherd et al. 2000; Lebrón et al. 2006).

MM-3 appears to be associated with the 8.4 GHz emission but does not have the detectable organic molecules indicative of a hot core. If the 8.4 GHz emission arises from an ultracompact (UC) H II region, the central star that photoionizes the circumstellar material should also give rise to high temperatures in the molecular gas. The absence of a hot core toward MM-3 indicates a relatively lower temperature in the molecular gas. This fact leads us to suggest that the faint 8.4 GHz emission likely arises from the ionized wind emission driven by an intermediate- to high-mass protostar in the MM-3 core. Although the ionized wind emission has been detected toward nearby low-mass young stars, the typical flux is on the order of 0.1 to a few mJy (Anglada et al. 1998). Such flux levels, after being scaled down by a factor of $10–100$ to account for distance, would not be detectable at the distance of AFGL 5142 at an rms of 0.09 mJy beam^{-1}. Thus, the ionized wind emission toward MM-3 is likely to be powered by a more massive young star. In a model in which the ionized emission arises from the plane-parallel shock when a neutral wind plows into high-density material, Curiel et al. (1989) derived a relation between the momentum rate in the outflow and the radio flux:

$$\frac{\dot{P}}{1 \, M_\odot \, \text{yr}^{-1} \, \text{km s}^{-1}} = \frac{10^{-3.5}}{\eta} \frac{S_\nu}{1 \, \text{mJy}} \left(\frac{d}{1 \, \text{kpc}}\right)^2 .$$

Here $\dot{P}$ is the momentum rate in the outflow and $\eta = 0.1$ is the efficiency factor corresponding to the fraction of the stellar wind that is shocked and produces the radio emission. For a flux S_ν of 0.35 mJy, we obtain an outflow momentum rate $\dot{P} = 4 \times 10^{-3} \, M_\odot \, \text{yr}^{-1} \, \text{km s}^{-1}$. This is in rough agreement with the outflow momentum rate in the CO outflow. In order to test our hypothesis on the ionized wind nature of CM-2, more sensitive centimeter continuum observations are needed to measure its spectral index.

Additional evidence that MM-3 is powered by an embedded massive star comes from the amount of circumstellar mass present. Although the total mass in MM-3 appears to be smaller as compared to MM-1 and MM-2, the mass estimates from the dust emission depend $(1/T)$ on the dust temperature assumed. We assumed a dust temperature of 45 K for MM-1 and MM-2. If we
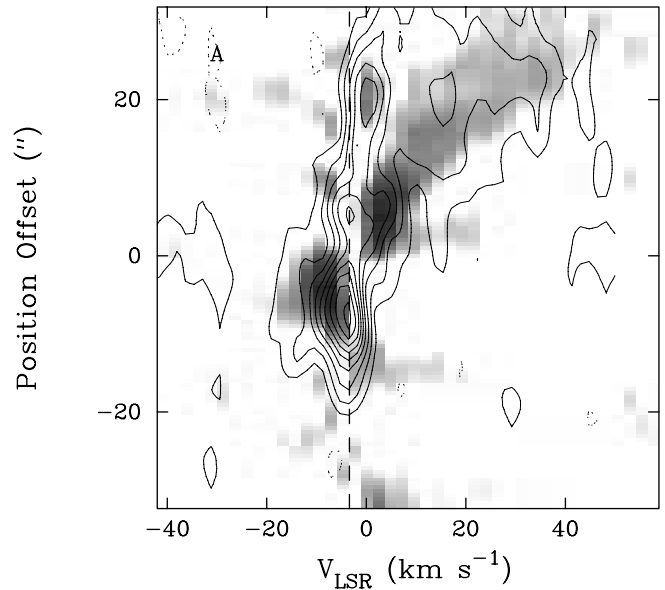

FIG. 9.—Emission from the SiO 2−1 line, from Hunter et al. (1999), in contours, overlaid on the ^{12}CO 2−1 emission, in grayscale, for outflow A. The cut of the position-velocity plot is along the outflow axis, with position offset from MM-2. The SiO emission is plotted in steps of 18 mJy beam^{-1}.

use a gas temperature of 250 K for MM-2, the mass in MM-2 would be 0.7 $M_\odot$, comparable to the mass in MM-3. Thus, many lines of evidence suggest that MM-3 is an intermediate-mass to massive star at an earlier evolutionary stage than MM-1 and MM-2. At such a stage, the radiation of the central star may not yet have produced a large enough core with high enough temperatures to render detection in hot-core molecules possible.

In addition to the strong dust peaks MM-1, MM-2, and MM-3, MM-4 coincides with the H_2O maser feature $3''$ to the east of the strong millimeter peaks. H_2O masers can be excited in dense envelopes ($\sim 10^8$ cm^{-3}) surrounding protostars through interaction with molecular outflows (Elitzur et al. 1989; Felli et al. 1992). Thus, the H_2O maser emission may indicate the presence of a fourth young star.

In contrast to the spatial agreement of a water maser with MM-4, a pair of H_2O masers lie near symmetrically $2''$ to the southeast and northwest of MM-5. There appears to be a high-velocity CO feature (see the channel maps at velocities from 4 to 8.8 km s^{-1} in Fig. 5b) aligned with this source. This CO feature can be part of outflow C associated with MM-1. On the other hand, it could also be a separate outflow associated with MM-5.

4.2. Kinematics and Driving Source of Outflows

Of the three molecular outflows identified in the CO and SO emission, outflow A coincides with a jetlike SiO outflow reported by Hunter et al. (1999). Figure 9 presents an overlay of the position-velocity diagram of the CO and the SiO emission along the axis of outflow A. For the SiO 2−1 line, strong emission appears around ±6 km s^{-1} from the cloud systemic velocity. Higher velocity emission is detected up to ±40 km s^{-1} from the cloud velocity near the position of the driving source; i.e., the position offset around $0''$. The maximum velocities of the SiO emission along the outflow axis increase with the distance from the driving source, similar to that of the CO outflow.

Outflowing gas moving faster than the sound speed in a cloud (a few km s^{-1}) produces shocks when interacting with the core material and enhances the gas temperature. As reported in Zhang et al. (2002), gas heating due to outflow A is seen in AFGL 5142.
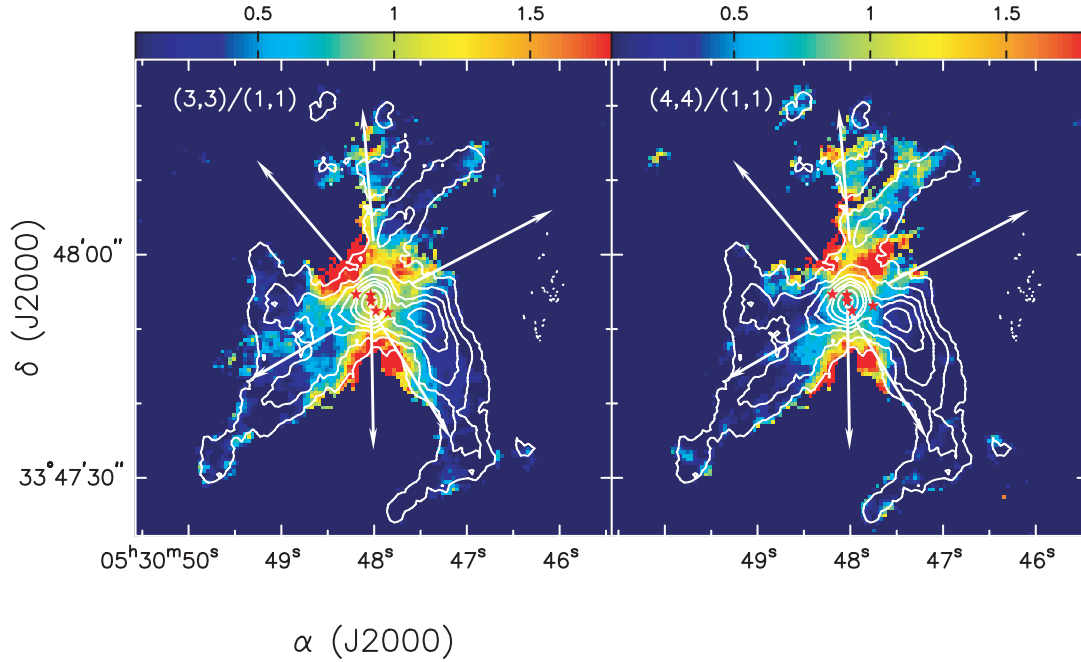
Fig. 10.—Ratios of the NH_3 $(J, K) = (3, 3)$ to $(J, K) = (1, 1)$ and NH_3 $(J, K) = (4, 4)$ to $(J, K) = (1, 1)$ emission (*color*), overlaid on the integrated emission of the NH_3 $(J, K) = (1, 1)$ line (*contours*). The images are taken from Zhang et al. (2002). The higher ratios denote higher temperatures. Arrows mark the three molecular outflows A, B, and C. The stars mark the positions of the millimeter continuum peaks MM-1, MM-2, MM-3, MM-4, and MM-5.

We reexamined the ratio of the NH_3 $(J, K) = (3, 3)$ and $(J, K) = (4, 4)$ lines to the $(J, K) = (1, 1)$ line presented in Zhang et al. (2002). Figure 10 shows the NH_3 ratio maps with all three outflows marked. The NH_3 $(J, K) = (1, 1), (3, 3)$, and $(4, 4)$ emission lines are from energy levels of 23, 125, and 230 K, respectively. Since upper (J, K) transitions arise from higher energy levels, the higher $(3,3)/(1,1)$ and $(4,4)/(1,1)$ ratios reveal warmer molecular gas. It is clear that in addition to the temperature enhancement along outflow A, there appears to be enhanced temperatures along outflows B and C.

All three outflows appear to originate from the central core of about $3''$ area. Therefore, it is difficult to identify the driving source. Using the data in this paper and the H_2O maser distributions and proper motions, we attempt to assign driving sources for the three outflows, with a caveat that the assignment may not be unique. There are three centimeter continuum peaks within the $3''$ region. CM-1A and CM-1B are separated by less than $0.2''$ and coincide with the 225 GHz continuum peak MM-1. The H_2O maser studies with the Very Long Baseline Array (VLBA) by Goddi & Moscadelli (2006) show a cluster of masers associated with CM-1A, CM-1B, and MM-1. The masers are concentrated to the northwest and southeast of the continuum source and exhibit proper motion along the axis of P.A. $= -40°$. This orientation is close to the axis of outflow C. Therefore, it is likely that MM-1 is the driving source of outflow C. The two centimeter continuum peaks toward MM-1 could be a close binary with a projected separation of 400 AU. On the other hand, CM-1A and CM-1B are aligned in a similar direction as the H_2O maser proper motion. It is more likely that the two centimeter peaks trace an ionized jet in the outflow.

For outflow B, both the CO and SO lobes (see the channel at -12.8 km s^{-1} in CO) appear to put MM-3 close to the geometric center. The H_2O maser study by Goddi & Moscadelli (2006) also detected a pair of maser spots at a similar position angle. However, the geometric center of the H_2O masers appears to be north of MM-3, closer to MM-2. This pair of masers was not detected in other VLA observations (Hunter et al. 1999); thus, their proper

motion may be questionable. We propose that MM-3 is the driving source of outflow B.

H_2O masers are also detected in the vicinity ($<0.5''$) of MM-2. This source, which is not detected at 8.4 GHz with the VLA at an rms of 0.09 mJy beam^{-1}, is associated with a hot core with strong CH_3CN emission. As it is the only dominant continuum source remaining, MM-2 probably drives the north-south outflow A.

4.3. *Chemical Variations*

The AFGL 5142 region reveals interesting variations in molecular line emission. SO emission is seen toward cores MM-1, MM-2, and MM-3, while CH_3OH, CH_3CN, OCS, and HNCO emission are detected only toward the two hot cores MM-1 and MM-2. This difference indicates that SO is abundant during a long period of core evolution from an early and relatively cold stage through a more evolved and warm/hot stage. On the other hand, CH_3OH and CH_3CN are abundant only when massive cores are more evolved, such that heating from the central protostar evaporates the molecules from the dust.

SO and CH_3OH emission are also detected toward molecular outflows away from the dense core. This is expected, as their abundances are enhanced in outflow shocks, where heating and UV radiation from shocks release CH_3OH and sulfur-bearing molecules from dust and enhance the formation of SO in the gas phase. The timescale of the abundance enhancement is 10^4 yr (Viti & Williams 1999), consistent with the dynamical timescale of the outflow.

4.4. *Cluster Star Formation*

The multiple centimeter and millimeter continuum sources identified in the AFGL 5142 region indicate a dense cluster in formation. The infrared imaging in the J, H, and K bands by Hunter et al. (1995) reveal 30 point sources with infrared (IR) excess over an area of $3'$. However, nearly all the IR sources lie outside of the dense core. The density of the IR sources within the 0.1 pc radius

from the millimeter continuum sources is about 10^3 stars pc^{-3}. This is much smaller than the average stellar density of $\lesssim 10^5$ pc^{-3} within the central 0.2 pc in the Orion Nebula, with 3 O stars within 0.1 pc (Hillenbrand 1997; Hillenbrand & Hartmann 1998). W3 IRS 5, a cluster with a total luminosity of $2 \times 10^5\ L_\odot$, has five near-IR sources within 5600 AU, equivalent to 6×10^5 stars pc^{-3}. Toward AFGL 5142, three protostars are revealed in the millimeter observations with a projected separation of 2.3″, or 4100 AU, which is equivalent to a stellar density of 2×10^5 stars pc^{-3}. Because the average is performed over a very small region, this high stellar density is not necessarily representative of the entire region. Nevertheless, the AFGL 5142 region appears to form a dense cluster. The luminosity for AFGL 5142 is 1–2 orders of magnitude smaller than that of the Orion Nebula and W3 IRS 5 and appears to harbor only early B stars. Unlike the Orion Nebula and W3 IRS 5, however, all three protostellar objects in AFGL 5142 appear to be actively accreting because of the presence of outflow activity. It is possible that they may become O stars when the star formation is complete.

Zhang et al. (2002) reported a velocity gradient and large NH$_3$ line width of 6.4 km s^{-1} toward the peak of the 3 mm continuum detected by Hunter et al. (1999). The kinematics in NH$_3$ appears to be consistent with a rotating disk in the region. Higher resolution observations with the SMA resolved the 3 mm dust peak into two sources separated by 1″, which excite two hot cores that are detected in CH$_3$CN emission. The two hot cores have systemic velocities of -1 and -3.4 km s^{-1}, which creates the velocity gradient seen in the NH$_3$ emission at lower resolution. Reexamining the data in Zhang et al. (2002), we found that at $\sim 1''$ resolution, the NH$_3$ (3,3) emission shows an elongation in the north-south direction. There appear to be two velocity components in the NH$_3$ (3,3) channel maps (see Fig. 2c in Zhang et al. 2002), consistent with the CH$_3$CN data. Refitting the 1″ resolution NH$_3$ (3,3) line yields a FWHM of $\gtrsim 6$ km s^{-1} for MM-1 and MM-2. The line width is still significantly larger than the typical NH$_3$ line width of 2 km s^{-1} in the extended emission. The increase of line width in NH$_3$ and CH$_3$CN is consistent with the enhanced infall/rotation in the circumstellar material surrounding the star. However, due to the dominance of the velocity shift between the MM-1 and MM-2 cores, no rotational motion toward the individual cores can be discerned over a scale of $>1''$.

The study of the AFGL 5142 region highlights the complex kinematics in cluster-forming regions where multiple massive stars compete for gravitational influence. In such an environment, extended rotating disks are likely truncated by tidal interactions. The relative motion of dense cores surrounding massive stars can dominate the kinematics and can even create false signals of rotation. High angular resolution observations in continuum and spectral lines are the key to understanding the kinematics in these regions.

Despite the complexity in the core, the molecular outflows seen in CO and SO at larger scales provide insight into the formation process of stars in the cluster environment. By physical connection, the well-collimated outflows indirectly suggest the presence of circumstellar accretion disks toward the three protostars in this cluster environment. One issue under debate in the past few years has been the formation mechanism of massive stars. In contrast to low-mass stars, for which stellar radiation exerts little dynamical influence on the infalling material, strong radiation from massive stars becomes a barrier to infall and may even prevent the formation of stars beyond $8\ M_\odot$ (Larson 1969; Larson & Starrfield 1971; Kahn 1974; Yorke & Krügel 1977; Wolfire & Cassinelli 1987). Several solutions have been proposed to alleviate this radiation problem. The most effective solution is a flattened accretion disk (Nakano 1989; Jijina & Adams

1996; Yorke & Sonnhalter 2002), which shields most infalling material from the stellar radiation. An additional benefit of a flattened disk is that photons can escape through the lower density region along the polar axis of the disk (Yorke & Sonnhalter 2002; Krumholz et al. 2005). All the above-mentioned solutions build on the notion that massive stars form through the gravitational collapse and disk accretion processes (McKee & Tan 2002; Keto 2003). Bonnell et al. (1998) and Bonnell & Bate (2002) put forward an alternative process in which massive stars form through multiple mergers/collisions of low-mass protostars. This coalescence model appears to circumvent the radiation problem, but it requires an exceedingly high stellar density ($\gtrsim 10^6$ stars pc^{-3}) in order for the process to be effective. In addition, the model still faces the radiation problem if the mechanical energy of the merging stars is released through radiation (Bally & Zinnecker 2005). These two schools of models can be tested by observations (Zhang 2005; Cesaroni et al. 2007). Unlike the infall/accretion model, the coalescence scenario does not produce well-collimated outflows from massive young stars (Bally & Zinnecker 2005). Our observations indicate that the coalescence model does not appear to be at work in this high-mass star formation region, since collimated outflows point to an alternative process; i.e., disk-mediated accretion. At the same time, the coalescence model requires a high stellar density ($\gtrsim 10^6$ pc^{-3}) for a merger to be effective. This stellar density requirement is not likely met in this region.

The coalescence scenario is a variation of the competitive accretion model (Bonnell & Bate 2002; Bonnell et al. 2004), in which a cluster of low-mass protostars with a common gravitational potential accretes the distributed gas from a reservoir of material in the molecular cloud. Protostars located near the center of the potential accrete at a higher rate because of the stronger gravitational pull and experience faster mass growth. This model explains the stellar initial mass function that is observed (Bonnell & Bate 2002; Bonnell et al. 2004). The main difference between turbulent accretion and competitive accretion is that in the former model protostars accrete gravitationally bound gas, whereas in the competitive accretion model massive protostars accrete mostly from gravitationally unbound gas. As a consequence, the competitive accretion model predicts that the final mass of massive stars does not correlate with the core mass (Bonnell et al. 2004). In addition, the accretion rate in the turbulent accretion model goes with the turbulent velocity V_t as V_t^3/G, while in the competitive accretion model the accretion rate goes as $4\pi\rho\left[(GM)^2\right]/V_t^3$ for Bondi-Hoyle accretion. Here G is the gravitational constant, ρ is the gas density, and M is the mass of the accreting star. We estimate the accretion rate using the parameters derived here. For $V_t = 2.5$ km s^{-1}, $M = 5\ M_\odot$, and $\rho = 10^5$ cm^{-3} (the mean density in the core), we find an accretion rate of $4 \times 10^{-3}\ M_\odot$ yr^{-1} for turbulent accretion and $2 \times 10^{-6}\ M_\odot$ yr^{-1} for Bondi-Hoyle accretion. The rate of $4 \times 10^{-3}\ M_\odot$ yr^{-1} is sufficiently high to account for the mass loss in the outflow, whereas the rate of $2 \times 10^{-6}\ M_\odot$ yr^{-1} appears to be too low to account for the mass loss rate in the outflow. On the other hand, the accretion rate is sensitive to turbulent velocity. The measured line width reported in Table 2 is probably affected by systematic motion (infall/rotation and outflow) in the core. If we assume a smaller value of $V_t = 1.5$ km s^{-1} on the basis of the NH$_3$ line width in the extended core (Zhang et al. 2002), we find an accretion rate of $8 \times 10^{-4}\ M_\odot$ yr^{-1} for turbulent accretion and $1 \times 10^{-5}\ M_\odot$ yr^{-1} for Bondi-Hoyle accretion. The latter value is still somewhat low, but it is closer to the accretion rate required for producing the observed outflows (Zhang et al. 2005). Although the test of the two models based on the AFGL 5142 data appears to be inconclusive, it is hopeful that future observations of massive cores at earlier evolutionary

stages will provide measurements of relevant physical parameters, especially turbulent velocity, and thus provide a more definitive test of the two models.

5. CONCLUSIONS

High-resolution ($1''$) observations with the SMA identified a high-mass protocluster in AFGL 5142. The 1.3 mm image reveals five continuum peaks with large variations in molecular line emission. Two millimeter cores, MM-1 and MM-2, are associated with the CH_3CN emission, with rotational temperatures of $\sim$90 and 250 K and abundances of 1×10^{-8} and 4×10^{-8}, respectively. The higher temperature and inferred high luminosity indicate that they likely constitute massive protostars. The remaining three cores do not have detectable CH_3CN and CH_3OH emission and likely harbor less massive (or less evolved) protostars.

The CO and SO emission reveal at least three possible molecular outflows. The terminal velocity of the CO emission reaches up to 50 km s^{-1}. The outflows have masses of 3 $M_\odot$ and momenta of 12–20 $M_\odot$ km s^{-1}, typical of outflows associated with high-mass stars. Both CO and SiO emission in the dominant outflow A have terminal velocities that increase with distance from the star. The presence of multiple collimated outflows in this protocluster provides indirect evidence that accretion is the dominant process for the formation of the massive protostars in this cluster.

REFERENCES

Anglada, G., Villuendas, E., Estalella, R., Beltrán, M. T., Rodríguez, L. F., Torrelles, J. M., & Curiel, S. 1998, AJ, 116, 2953
Bachiller, R., Pérez Gutiérrez, M., Kumar, M. S. N., & Tafalla, M. 2001, A&A, 372, 899
Bally, J., & Zinnecker, H. 2005, AJ, 129, 2281
Beuther, H., et al. 2004a, ApJ, 616, L19
———. 2004b, ApJ, 616, L31
Bonnell, I. A., & Bate, M. R. 2002, MNRAS, 336, 659
Bonnell, I. A., Bate, M. R., & Zinnecker, H. 1998, MNRAS, 298, 93
Bonnell, I. A., Vine, S. G., & Bate, M. R. 2004, MNRAS, 349, 735
Ceccarelli, C., Loinard, L., Castets, A., Tielens, A. G. G. M., & Caux, E. 2000, A&A, 357, L9
Cesaroni, R., Felli, M., Jenness, T., Neri, R., Olmi, L., Robberto, M., Testi, L., & Walmsley, C. M. 1999, A&A, 345, 949
Cesaroni, R., Galli, D., Lodato, G., Walmsley, C. M., & Zhang, Q. 2007, in Protostars and Planets V, ed. B. Reipurth, D. Jewitt, & K. Keil (Tucson: Univ. Arizona Press), 197
Chandler, C. J., Brogan, C. L., Shirley, Y. L., & Loinard, L. 2005, ApJ, 632, 371
Chen, H.-R., Welch, W. J., Wilner, D. J., & Sutton, E. C. 2006, ApJ, 639, 975
Chen, Y., Yao, Y., Yang, J., Zeng, Q., & Sato, S. 2005, ApJ, 629, 288
Choi, M., Evans, N. J., & Jaffe, D. T. 1993, ApJ, 417, 624
Curiel, S., Rodriguez, L. F., Bohigas, J., Roth, M., Canto, J., & Torrelles, J. M. 1989, Astrophys. Lett. Commun., 27, 299
Elitzur, M., Hollenbach, D. J., & McKee, C. F. 1989, ApJ, 346, 983
Estalella, R., Mauersberger, R., Torrelles, J. M., Anglada, G., Gomez, J. F., Lopez, R., & Muders, D. 1993, ApJ, 419, 698
Felli, M., Palagi, F., & Tofani, G. 1992, A&A, 255, 293
Goddi, C., & Moscadelli, L. 2006, A&A, 447, 577
Gueth, F., & Guilloteau, S. 1999, A&A, 343, 571
Herbst, E., & Leung, C. M. 1990, A&A, 233, 177
Hildebrand, R. H. 1983, QJRAS, 24, 267
Hillenbrand, L. A. 1997, AJ, 113, 1733
Hillenbrand, L. A., & Hartmann, L. W. 1998, ApJ, 492, 540
Ho, P. T. P., Moran, J. M., & Lo, K. Y. 2004, ApJ, 616, L1
Hunter, T. R., Testi, L., Taylor, G. B., Tofani, G., Felli, M., & Phillips, T. G. 1995, A&A, 302, 249
Hunter, T. R., Testi, L., Zhang, Q., & Sridharan, T. K. 1999, AJ, 118, 477

Jijina, J., & Adams, F. C. 1996, ApJ, 462, 874
Kahn, F. D. 1974, A&A, 37, 149
Keto, E. 2003, ApJ, 599, 1196
Krumholz, M. R., McKee, C. F., & Klein, R. I. 2005, Nature, 438, 332
Kuan, Y.-J., et al. 2004, ApJ, 616, L27
Lada, C. J., & Fich, M. 1996, ApJ, 459, 638
Larson, R. B. 1969, MNRAS, 145, 271
Larson, R. B., & Starrfield, S. 1971, A&A, 13, 190
Lebrón, M., Beuther, H., Schilke, P., & Stanke, T. 2006, A&A, 448, 1037
McKee, C. F., & Tan, J. C. 2002, Nature, 416, 59
Nakano, T. 1989, ApJ, 345, 464
Pestalozzi, M. R., Minier, V., & Booth, R. S. 2005, A&A, 432, 737
Scoville, N. Z., & Kwan, J. 1976, ApJ, 206, 718
Shepherd, D. S., Yu, K. C., Bally, J., & Testi, L. 2000, ApJ, 535, 833
Slysh, V. I., Dzura, A. M., Val'tts, I. E., & Gerard, E. 1997, A&AS, 124, 85
Snell, R. L., Huang, Y.-L., Dickman, R. L., & Claussen, M. J. 1988, ApJ, 325, 853
Su, Y., Zhang, Q., & Lim, J. 2004, ApJ, 604, 258
Swade, D. A. 1989, ApJ, 345, 828
Torrelles, J. M., Gómez, J. F., Anglada, G., Estalella, R., Mauersberger, R., & Eiroa, C. 1992, ApJ, 392, 616
Viti, S., Girart, J. M., Garrod, R., Williams, D. A., & Estalella, R. 2003, A&A, 399, 187
Viti, S., & Williams, D. A. 1999, MNRAS, 310, 517
Wilner, D. J., Wright, M. C. H., & Plambeck, R. L. 1994, ApJ, 422, 642
Wolfire, M. G., & Cassinelli, J. P. 1987, ApJ, 319, 850
Yorke, H. W., & Krügel, E. 1977, A&A, 54, 183
Yorke, H. W., & Sonnhalter, C. 2002, ApJ, 569, 846
Zhang, Q. 2005, in IAU Symp. 227, Massive Star Birth: A Crossroads of Astrophysics, ed. R. Cesaroni, M. Felli, E. Churchwell, & M. Walmsley (Cambridge: Cambridge Univ. Press), 135
Zhang, Q., Ho, P. T. P., & Ohashi, N. 1998, ApJ, 494, 636
Zhang, Q., Ho, P. T. P., & Wright, M. C. H. 2000, AJ, 119, 1345
Zhang, Q., Ho, P. T. P., Wright, M. C. H., & Wilner, D. J. 1995, ApJ, 451, L71
Zhang, Q., Hunter, T. R., Brand, J., Sridharan, T. K., Cesaroni, R., Molinari, S., Wang, J., & Kramer, M. 2005, ApJ, 625, 864
Zhang, Q., Hunter, T. R., Sridharan, T. K., & Ho, P. T. P. 2002, ApJ, 566, 982